



In situ observation of the impact of hydrogen bubbles in Al–Cu melt on directional dendritic solidification

T. Werner^{1,*} , M. Becker¹ , J. Baumann¹ , C. Pickmann² , L. Sturz² , and F. Kargl¹

¹Institut für Materialphysik im Weltraum, Deutsches Zentrum für Luft- und Raumfahrt (DLR), 51170 Köln, Germany

²ACCESS e.V., 52072 Aachen, Germany

Received: 9 September 2020

Accepted: 28 December 2020

Published online:
18 January 2021

© The Author(s) 2021

ABSTRACT

Much research has already been focused on the solid-bubble interaction in the interdendritic space for solidifying materials. However, commonly, bubble nucleation is not limited to the mushy zone but also occurs in the liquid melt. In the present research on an Al-10%wt.Cu alloy, the interaction between these bubbles and the approaching solidification front becomes apparent under in situ X-radiography and allows for new insights into the influence of bubbles on the solidifying microstructure. The observed effects comprise bulging of the solidification front toward the bubble, bending of dendrites in front of the bubble, coronal outgrowths surrounding the bubbles, as well as bubble growth, bubble pushing, and bubble eruption. It is found that for the present Al–Cu alloy, the local variation in the solidification speed can be attributed to the bubbles' insulating properties. The range of this effect was observed to be up to 900 μm, depending on the bubble diameter, locally increasing solidification speed by up to 350%. The influences of Marangoni vortices and coronal nucleation of misoriented dendrites around bubbles on the homogeneity of the microstructure are discussed. A comparison with experiments on model alloys and simulations from various other studies highlights the similarities and differences to this metallic alloy system.

Introduction

Since the earliest days of metalworking, pores have been known to reduce the mechanical stability of workpieces [1]. For that reason, the focus of the

metallurgical community has long since been cast onto nucleation and growth of gas bubbles in the interdendritic space [2–11], as well as their interaction with the dendrites surrounding them [6–9, 11–13].

Simulations, such as the work by Han et al. [2], predict wave-like nucleation and distribution of

Handling Editor: P. Nash.

Address correspondence to E-mail: Thomas.Werner@dlr.de

pores in the solidifying material or were developed to model the growth of various different types of porosity (microporosity, macroporosity, and shrinkage) simultaneously as shown in the research of Pequet et al. [3]. Even the development of large interdendritic pore networks and their relationship to the pore curvature were the focus of modeling by Felberbaum and Rappaz [11].

But not only simulations have yielded results on the topic of porosity-solid interaction; over the years, especially in situ imaging setups have established themselves as the primary means for observing the solidification process. Lee and Hunt, pioneering in situ X-radiography imaging for analysis of metallic samples in 1997, observed the formation of pores in aluminum (Al)–copper (Cu) alloys and characterized interdendritic pore morphology as a function of temperature [12]. A change of pore morphology was identified by Arnberg and Mathiesen and related to constraints by surrounding dendrites [4]. In 2016, Murphy et al. described the fragmentation of dendrites and ensuing columnar to equiaxed transition caused by bubbles in the mushy zone, as well as the effect of bubbles on intergranular spacing [13].

However, bubble nucleation is not limited to the interdendritic region. In the melt, impurities such as oxide particles can lead to heterogeneous nucleation of gas bubbles [14]. These bubbles can escape due to buoyancy, be engulfed by the dendritic front, or push away/re-melt the dendritic network [6, 13, 15]. Thus, the need arises to better understand the interaction between those pre-existing bubbles in the melt and the solidifying material. In particular, the advantages of in situ imaging compared to postmortem analysis, when examining such interactions at an early solidification stage, are apparent: The whole process can immediately be observed via the live-feed of the camera, clearly depicting the complete sequence of solidification events in real time. Simulations on metallic alloys and observation of transparent, organic model alloys have shown a notable influence of gas-bubbles on the solidification behavior of the material for this specific scenario of bubbles in front of the mushy zone.

Considering bubbles in the liquid in front of the solidifying material, Sekhar and Trivedi suggested localized variations in the solidification velocity due to concentration differences in the melt in the vicinity of pre-existing bubbles for a transparent organic model alloy [16]. A simulation of a metallic alloy by

Catalina et al., on the other hand, predicted the dominant effect on the solidification speed to be thermal insulation: The reduced heat flow through the gas, when compared to the liquid metal, would cause the melt on the solid-facing side of the bubble to be colder than the melt without bubble, and thus induce a localized increase in solidification speed [17].

Other simulation studies advocate the development of Marangoni flow fields surrounding the bubble. This interfacial effect, driven by a gradient in surface tension around the bubble, transports hot melt toward the dendrite front, causing bending of the dendrites. Corresponding experiments on a transparent organic succinonitrile-based alloy were performed by Nabavizadeh et al. in microgravity aboard the International Space Station, so as to eliminate gravity-driven factors such as convective flow and buoyancy of bubbles. The study concludes that Marangoni flow indeed affects the growth direction of dendrites, causing them to bend away from the bubble [18].

A third type of influence on the microstructure was observed by Han and Trivedi in 1994 and discussed in-depth by Xing et al. in 2012, both for succinonitrile-based transparent alloys [19, 20]. The solidifying material, upon coming into contact with the bubble, produced corona-shaped outgrowths along the gas-melt interface, which eventually evolved into dendrites growing along the temperature gradient.

With the focus on these three effects—bulging of the solidification front, deviation of dendrites due to Marangoni flow, and coronal outgrowths—the present work analyzes how pre-existing bubbles cause non-homogeneity of the growth and microstructure in an Al–Cu alloy. In situ X-radiography allows for direct observation of the directional columnar dendrite growth of the Al-10 %wt. Cu alloy sample processed in a Bridgman–Stockbarger-type furnace. To minimize buoyancy of the bubbles and grains, a sheet-like sample was processed in horizontal position, i.e., the gravity vector is orthogonal to the plane of the thin (near-2D) sample.

Different hydrogen (H) contents of the metallic samples have been achieved through the use of a gas-loading furnace [21]. Deformation of the dendrite front, growth direction of the dendrites, and morphological homogeneity will be discussed, as will be correlations between bubble diameter, distance range

of the insulating effect of bubbles and increase in solidification velocity near bubbles.

Similarities and differences between the present research and the aforementioned models will be addressed.

Experimental methods

Sample preparation

The good contrast in X-radiography between the Al-dendrites and the melt [15, 22, 23], as well as the alloy's property of H being the only soluble gas in it [14, 24, 25], ruling out chemical effects such as oxidation at the bubble-melt interface, are the underlying considerations for using the Al–Cu system.

More specifically, this study is based on an Al-10%wt. Cu alloy, the element ratio at which the alloy is density-matched [26]. At this elemental composition, the solidified Al has nearly the same density as the surrounding melt, and thus the influence of buoyancy effects is minimized.

To achieve reproducible gas-bubble numbers, Al-10%wt. Cu bulk samples were cast in a gas-loading furnace following the procedures described in [21]. Melting the alloy's raw materials in a well-defined environment (pressure, temperature) before introducing an atmosphere of controlled H-content, the liquid metal was then held for a defined amount of time at maximum temperature, before being cast in a steel-die acting as mold and heat-sink. By varying these four parameters (pressure, temperature, holding time at maximum temperature, and loading-gas concentration in the atmosphere), specimens with an H-content of $5.4 \cdot 10^{17}$ atoms/g (25.48 ppma) and $2.7 \cdot 10^{17}$ atoms/g (12.70 ppma) were produced. The gas contents for comparable Al-10%wt. Cu alloys used in other studies vary between $5.3 \cdot 10^{15}$ atoms/g and $5.4 \cdot 10^{17}$ atoms/g, situating the present work toward the upper end of the H-content spectrum [11, 12, 21, 27, 28]. The divergence of values by up to two orders of magnitude can be attributed to different casting and cooling conditions or to diverse methods of evaluation and shows the necessity for a controlled gas-loading process, as was already discussed elsewhere [21].

A short overview over the state of the art of H-charging of Al-alloys is given in Table 2 in the supplemental data, summarizing publications from 1989

to 2020 and situating the present work among them. Furthermore, as the literature sources give H-content in varying units [17, 21, 29–31], Equations (1–3) in the supplemental data provide the conversion for results in different units ([atoms/g], [ccm/100g]_{STP}, [ppma], and [ppmw]).

To prepare the samples for the X-ray investigations, the cast bulk samples were cut at a distance of 10 mm from the bottom face of the casting mold and ground according to ASTM standard E3-1115 to dimensions of 5 mm x 50 mm x 150 μm [32]. The cutting was performed on a Buehler Isomet4000 Linear Precision Saw equipped with a Buehler MetAbras abrasive cutoff wheel at 1700 rpm and a feed-rate of $1.2 \text{ mm} \cdot \text{min}^{-1}$. Subsequently, the sheet-like specimens were manually coated in boron-nitride (BN) spray (HeBoCoat 401E provided by Henze Boron Nitride Products AG) to avoid chemical interactions with the quartz-glass crucible. Due to the manual coating process, variations in the BN-layer thickness can cause darker patches overlaying the X-ray images. An in-depth description of the sample preparation process can be found elsewhere [21, 33].

In situ directional solidification experiments

To allow for in situ observation of the microstructural solidification process, the experiments were carried out in a Bridgman–Stockbarger furnace featuring an X-radiography unit as shown in Fig. 1. Taking into account the detector's native pixel size of 9 μm, as well as the sevenfold magnification resulting from the distance ratio of source/detector to source/sample, the effective pixel size of the setup amounts to 1.3 μm. A more in-depth description of the experimental unit can be found elsewhere [33]. Due to the thin (150 μm) sample geometry, the microstructure can be distinctly observed, as the dendrites usually do not superimpose each other, while at the same time, convective flow and buoyancy are reduced. It has been shown that the geometrical constraints in the nearly two-dimensional specimen, if oriented horizontally, effectively restrict gravitational effects such as buoyancy on bubbles and dendrites, and, to a certain extent, convection [22, 34].

It should be noted, however, that while horizontal orientation of the sample prevents bubble and dendrite movement caused by buoyancy effects and reduces thermal convection to a negligible level, according to Nguyen-Thi et al. it does not eliminate

solvent convection to a point identical to real microgravity [22]. For stable thermal and solutal conditions, vertical upward solidification reduces solutal convection further but results in buoyancy effects acting on bubbles and dendrites. As the present study requires immobile bubbles, the horizontal orientation was chosen.

An air-atmosphere of 1013.25 hPa (1 atm) ensured sufficient pressure to slow the degassing of H down to resolvable levels while taking into account the chosen frame rate of 0.54 Hz. The constant temperature gradient across the 6-mm-wide adiabatic gap was established between two heaters (ceramic glow igniters encased in heat resistant steel) as described by Zimmermann et al. [33]. For the directional solidification experiments, the samples were first thermally stabilized for 10 min, followed by a horizontal displacement of the sample inside of the furnace (which is mounted in place) at defined velocities for each specimen as shown in Table 1.

To ensure statistical significance, a total of four distinct samples (two with a lower H-concentration and two with a higher H-concentration), processed at two different pulling speed and thermal gradient combinations, were analyzed over five melting/solidification cycles as can be seen in Table 1. Pulling speed and thermal gradient were not found to have significant influence on the behavior of bubbles and will not be further discussed in this work.

Results

During the solidification process, H-bubbles are observed to nucleate and remain in the melt in front of the solidifying material until they either pop or are engulfed by the solidification front. In the latter case, for about 25% of these gas bubbles, deformation of the solid–liquid interface is observed in the immediate proximity of the bubble. This behavior was found in both, dendritic and planar fronts. Figure 2 shows a sequence of X-ray images taken from a specimen with an H-content of $2.7 \cdot 10^{17}$ atoms/g, starting at the beginning of solidification. Development of the localized deformation continues until the bubble is half-engulfed by the crystallites. Growth of the gas bubble correlating with the decreasing distance to the solidification front can be observed: Bubbles far away from the solidification front also grow, but at a much

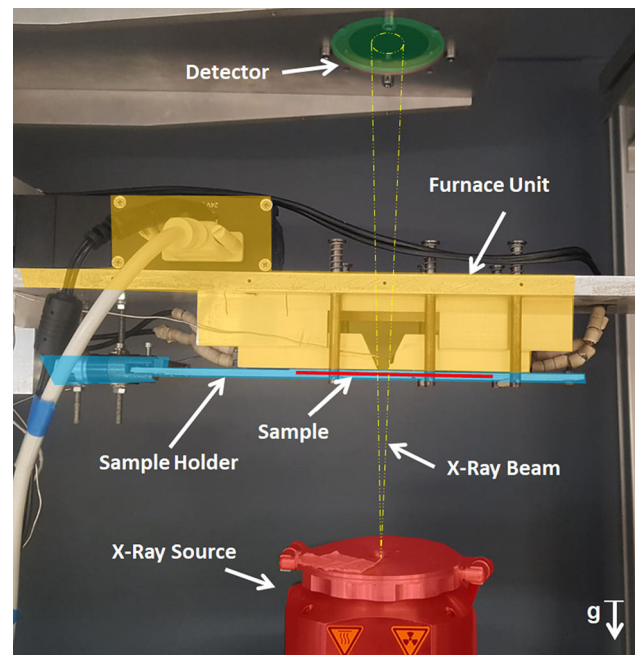


Figure 1 Setup of the gradient furnace. The furnace unit consists of two heaters (ceramic glow igniters encased in heat resistant steel) providing a constant temperature gradient across the adiabatic gap in between the two sides of the unit. The sample coated with boron nitride and encased in quartz glass can be moved along the adiabatic gap with a microstep motor. At the height of the adiabatic gap, the X-ray beam traverses the sample, before reaching the detector. g is the direction of the gravitational force. Color overlays distinguish the different main parts of the facility from each other in the image only.

slower rate than the bubbles close to the crystallizing solid, as seen in Fig. 3a and b. The gas-bubble is then pushed upwards, followed by sudden acceleration and eventually popping of the bubble. It has to be noted that the five described effects of the bubble growing, being pushed, being engulfed, accelerating, and popping are not commonly all occurring in an individual instance of the solidification front's bulging. In most observed cases, only one or two of the aforementioned phenomena would be observed.

As seen in Fig. 4a, relating the range of the bulging effect, quantified by d_{flat} (the shortest distance between the bubble and the solid–liquid interface for which the solidification front is still flat and has not shown any deformation), to the bubble diameter D (the diameter at the moment of first deformation of the solidification front) in the aforementioned situation, it was found that with increasing bubble diameter, the range of the effect also increases.

Table 1 List of processed specimens and their solidification parameters

Sample	Gas content [10^{17} atoms \cdot g $^{-1}$]	Solidification speed [$\mu\text{m} \cdot \text{s}^{-1}$]	Gradient [K \cdot mm $^{-1}$]
Sample 1	2.7	30	10
Sample 2	2.7	10	20
Sample 3	5.4	30	10
Sample 4_1	5.4	30	10
Sample 4_2	5.4	10	10

Similarly, the growth speed v_{\max} of the fastest growing dendrites near the gas bubble scales with d_{flat} and D . However, two distinct growth speed regimes are observed in Fig. 4a:

- For $D > 150 \mu\text{m}$, v_{\max} shows an overall trend to increase with D , but shares a negative correlation with d_{flat} .
- For $D < 150 \mu\text{m}$, the data shows no clear correlation.

The increase in solidification speed (in %) of v_{\max} compared to the local mean solidification speed of the solidification front is plotted in Fig. 4b. The graph illustrates the relation to bubble size and bubble distance to the front: The larger the bubble and the closer to the growth front, the higher the growth speed.

This effect can be observed for both H-concentrations of $5.4 \cdot 10^{17}$ atoms/g and $2.7 \cdot 10^{17}$ atoms/g. With higher H-content, the number of observable events increases accordingly.

Another phenomenon observed in this study, shown in Fig. 5, is the deviating/bending of dendrites prior to coming into contact with the H-bubble. Due to the high brightness of the bubble and the lower contrast of dendrites compared to the melt, this effect is most clearly observed on bubbles that pop while being engulfed by the solidification front.

However, instead of bending and bypassing the bubble, the dendrites can also be stopped by the bubble or come into direct contact with it at a certain distance off-center but without stopping. The bubble, as shown in Fig. 6a, upon experiencing immediate collision with a growing dendrite, then sees a corona-shaped layer of outgrowths forming at the bubble-melt interface and growing into the melt. These outgrowths quickly begin to orient themselves and eventually develop dendrites either growing in the same direction as the initial crystallites or deviating and forming a new grain (see Fig. 6b). However, even for the case that no new grain develops, a circular

region of about twice the bubble diameter surrounding the pore remains misoriented with respect to the columnar microstructure in its vicinity.

It should be noted that despite the original dendrites growing at an angle of about 45° , as seen in Fig. 6, the tips of all dendrites were observed to advance at the same speed, effectively resulting in an upward-growing solidification front.

To summarize the observations, the novelty of the presented findings in this work lies in the observation of three effects that had not previously been documented experimentally for metals: bulging of the solidification front close to bubbles in the melt, bending/deviation of dendrites around gas-bubbles, and coronal outgrowths nucleating around bubbles.

Additionally, five secondary phenomena appeared, notably bubble growth, bubble pushing, bubble engulfment, bubble “eruption”, and bubble popping, that will be briefly explained in the following section, for the convenience of the reader.

Discussion

Bulging of the solidification front

When discussing the deformation of a solidification front, the Mullins–Sekerka instability is often at the root of the effect: The solidification front randomly develops an irregularity/a bulge of atomic scale, which locally increases the thermal gradient and thus accelerates the growth of the initial bulge. This in turn leads to a self-amplifying scenario, which only slows down once the Gibbs–Thomson effect restricts the growth speed due to the surface curvature becoming too large to sustain for the system. That is what eventually results in the formation of dendrites [35, 36]. However, in the present case, deformation of the solidification front does not appear randomly but is only observed close to bubbles. It shows no periodicity and affects a segment of the solidification

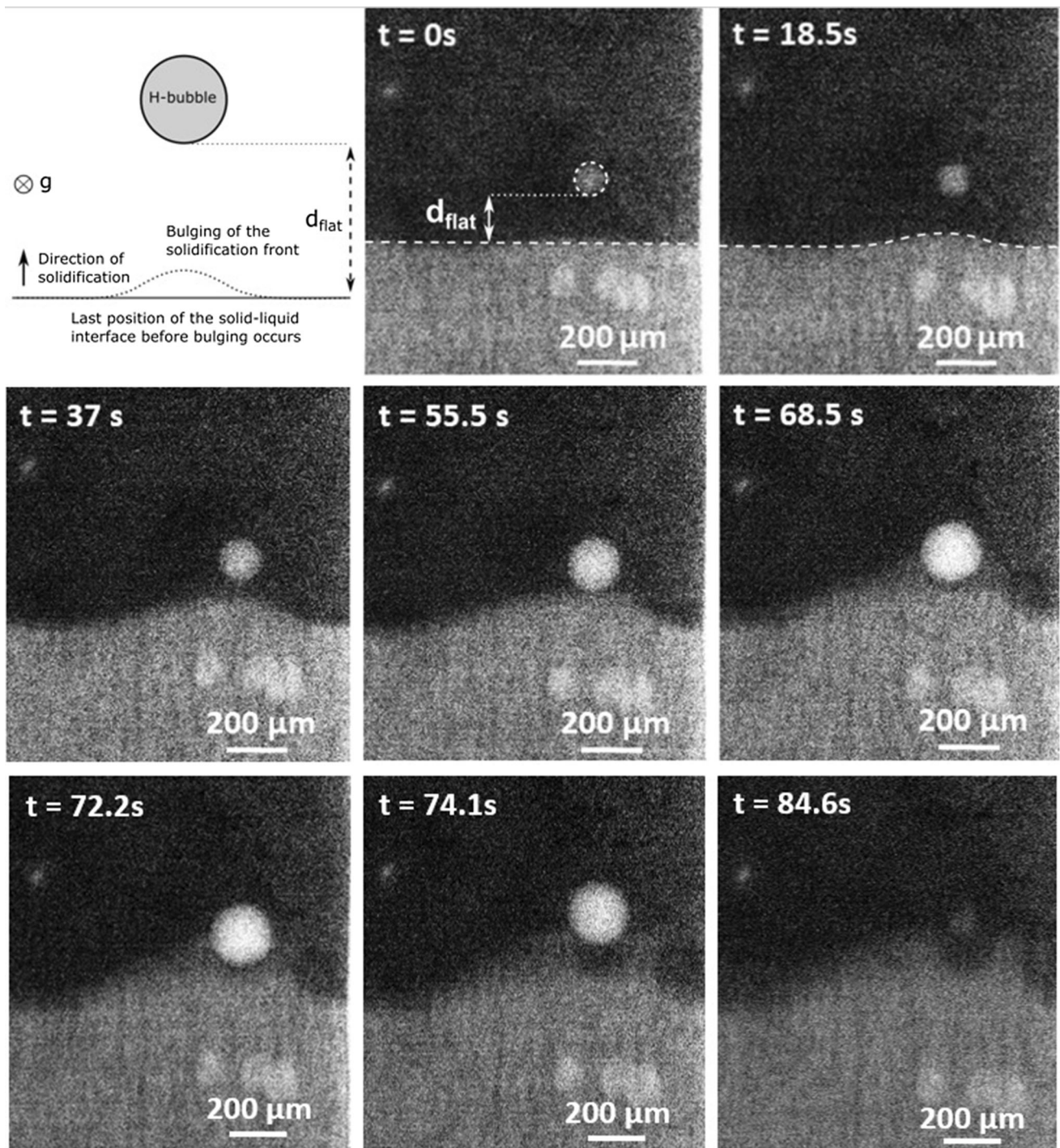


Figure 2 X-radiography image sequence of the upward-moving solidification front in sample 2, bulging out in the vicinity of a gas bubble in the Al-10%wt. Cu melt. The length d_{flat} represents the shortest distance between bubble and solidification interface for which the interface is still flat and has not shown any bulging. Bubble growth can be observed, as well as a slight displacement

where the bubble is pushed away by the approaching solid, leaving behind a U-shaped dent in the bulged-out solidification front. Between $t = 72.2\text{s}$ and $t = 74.1\text{s}$, the bubble suddenly accelerates and moves away from the surrounding crystalline material toward the hot end before popping. In all images, gravity acts orthogonally through the image plane.

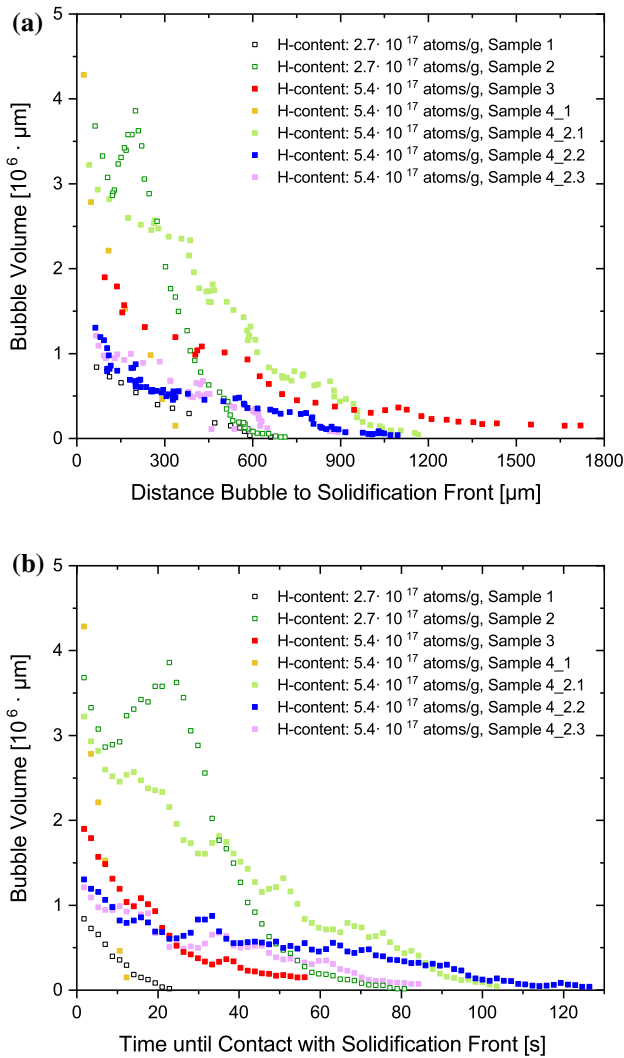


Figure 3 The growth of bubbles from five different heating/solidification cycles was evaluated as a function of **a** the distance to the solid and **b** time. In all cases, the volume of H-bubbles increases with decreasing distance to the solidification front and with longer duration of the experiment. For the computation of the bubble volume from the 2D data, perfectly spherical bubble geometry was assumed for $D < 150 \mu\text{m}$ (thickness of the sample). For larger bubbles, the spherical caps were subtracted symmetrically. In sample 2, the observed bubble moved and subsequently shrank when the solidification front was about $200 \mu\text{m}$ away, before starting to grow again. Different amounts of solved H, specifically $5.4 \cdot 10^{17}$ atoms/g (solid squares) and $2.7 \cdot 10^{17}$ atoms/g (empty squares), do not affect this behavior, only the amount of observable events.

front of up to several hundred microns for a single bulge, depending on the size of the bubble, as shown in Fig. 4.

The impact of the bubble on the crystallizing solid can be explained as follows: Considering gas bubbles

as particles with ideal insulating properties, the melt on the solid-facing side of the bubble is de facto colder than the melt at the same distance from the solid but far away from the bubble. This local temperature gradient will thus cause a deformation of the solidification front, in other words, an increase in growth speed of the crystallites closest to the bubble. The insulating effect and resulting temperature gradient both increase with bubble size. This is supported by the finding that larger bubbles have a greater impact on the growth speed increase as well as a bigger zone of influence (characterized by d_{flat}). This effect has already been discussed in multiple works focusing on simulation [17, 37, 38], and now, having observed it in situ, we can support these simulations with experimental evidence for a metallic material as shown in Fig. 2.

The discrepancy to Sekhar and Trivedi’s results [16], who found that bubbles lead to a depression in the solid–liquid interface, can be explained by the difference in experimental setups: While both their work and the present study use glass crucibles (thermal conductivity in the range of $0.8 \text{ W} \cdot (\text{m} \cdot \text{K})^{-1}$ [39]), their work focuses on succinonitrile-based organic alloys with a thermal conductivity of around $0.3 \text{ W} \cdot (\text{m} \cdot \text{K})^{-1}$ [40], while the present work features an Al–Cu alloy (thermal conductivity around $80 \text{ W} \cdot (\text{m} \cdot \text{K})^{-1}$ [41]). The heat flow through the sample itself is thus about 2.6 orders of magnitude higher in the present experiment than in Sekhar and Trivedi’s study, and accordingly, the thermal effects through the sample are more pronounced. Another experimental difference is found in the alloy composition: Sekhar and Trivedi used a solution of 5%wt. succinonitrile-95%wt. water (succinonitrile-phase crystallizes), whereas the present alloy composition amounts to 90%wt. Al-10%wt. Cu (Al-phase develops). The amount of rejected solute upon solidification is thus more than nine times as large in Sekhar and Trivedi’s experiments, and concentrational effects such as solute pile-up are more prominent in their study.

Except for the material used in the experiments, the geometry of the setup also influences the results to a certain point; specifically, the systematic error of 2D simulations and near-2D experiments needs to be kept in mind: as shown in Fig. 2b, for bubble diameters smaller than $150 \mu\text{m}$ (thickness of the sample), the increase in growth speed of dendrites compared

to the speed of the advancing solidification front becomes smaller with increasing bubble size. This effect can be attributed to the bubble acting as an obstruction for the Al-rich melt feeding the growing crystallites. For small bubbles, the melt can still flow past the bubble, on its sides as well as above or below it. The bigger the bubble, the smaller the gap between sample surface and bubble becomes. This, however, changes at $D > 150 \mu\text{m}$, when the bubble connects the top and bottom faces of the sample. All melt is forced to flow around the sides of the bubble, and regardless of the bubble size, the flow rate stays the same from then on.

The bulging effect has been observed for 25% of the bubbles in the present setup. This observation rate is attributed to the growth and popping events that happen throughout the experiment, as well as the geometrical position in thickness-direction of the bubbles relative to the growing dendrites that cannot be determined in this near-2D setup: If a bubble is adhering to the top side of the sample, but the dendrites grow closer to the bottom side of the sample, the growth direction is not blocked and only minimal interaction is possible.

Bending of dendrites

The observed bending of the dendrites' growth direction away from the bubble could be attributed to the Marangoni effect. The Marangoni effect is an interfacial phenomenon that induces fluid transport along an interface following a gradient in surface tension. The fluid is transported from a region of lower surface tension toward a region of higher surface tension. In the case of a spherical interface in an almost-2D setup, this would lead to the formation of two vortices on the outside of the sphere, as depicted in Fig. 7. The direction of these flow vortices depends on two main factors: The concentration gradient of the solute being different due to dendrite growth locally enriching the melt in one element (here Cu), and the temperature difference already mentioned in "Bulging of the solidification front" section.

While the temperature gradient will always cause a flow from the hot side of the bubble to the cold side, the concentration gradient-driven flow depends on the melt compositions and the corresponding surface tension distribution around the bubble. Depending on the thermal/concentrational gradients of the system, the flow vortices can thus transport fluid in

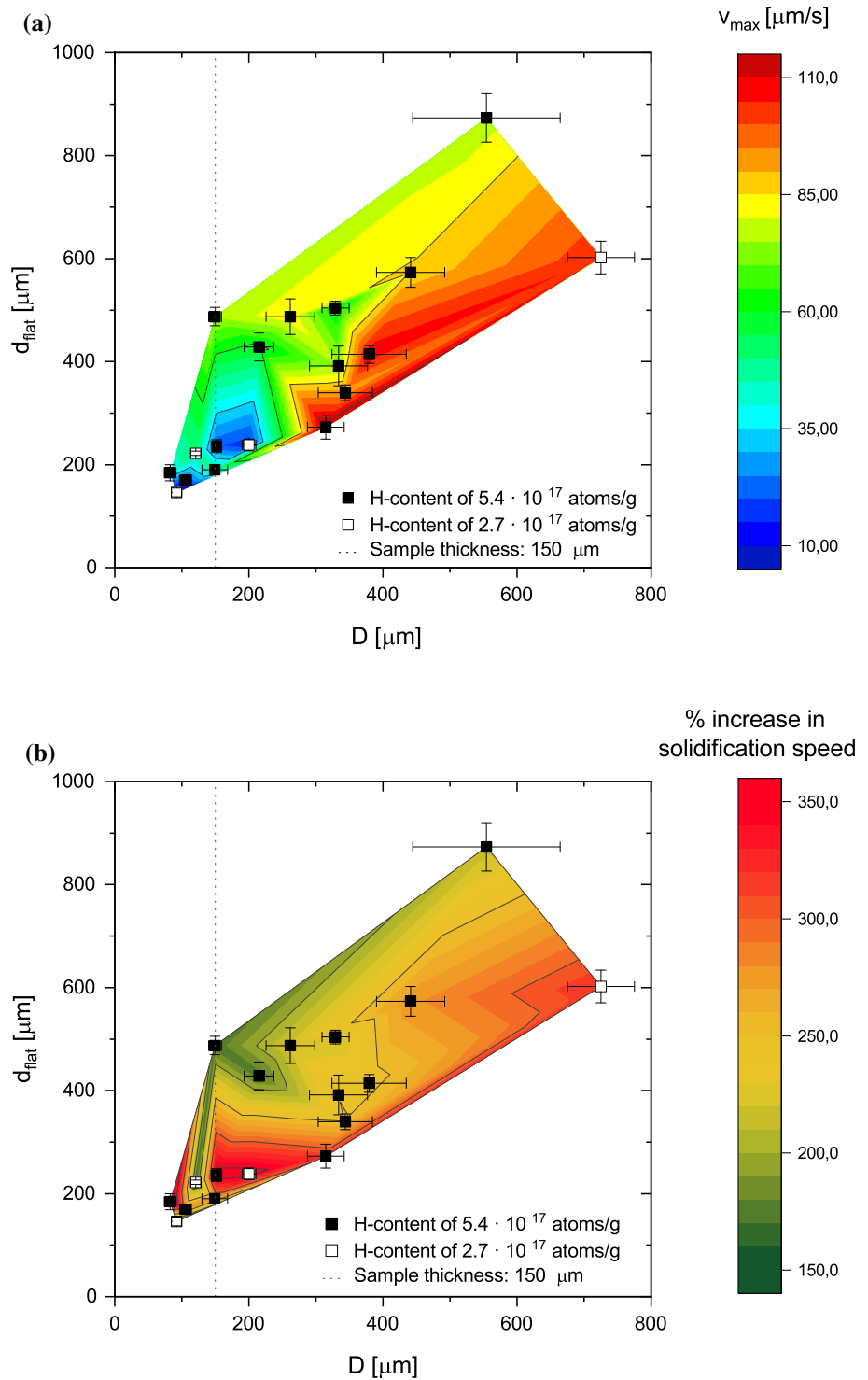
either direction for different experimental setups [4, 18, 42, 43].

In the case of Al–Cu alloys, the surface tension increases with both increasing Cu-content and decreasing temperature [44]. In the free melt (ahead of the mushy zone), the concentration of Cu is highest close to the solidification front. Additionally, on the dendrite-facing side of the bubble, the temperature is lower than on the melt-facing side, similarly causing the surface tension to be higher. As both parameters cause an increase in surface tension on the dendrite-facing side of the bubble, Marangoni vortices will transport Al-rich, hot melt toward the dendrite front. This causes a deviation of the dendrites' growth direction away from the bubble under microgravity conditions, according to Nabavizadeh et al. [18].

Under standard gravity, convective effects as well as movement of the bubbles due to buoyancy make it challenging to observe the Marangoni effect on bubble interfaces [18]. As the near-2D setup of the experiment in horizontal position reduces both, convection and buoyancy-effects, Marangoni flow fields may be strong enough to influence the growing microstructure in an observable way. However, it cannot be determined with absolute certainty if the bending of the dendrites close to the bubbles, as observed in the present study, is due to the Marangoni flow or due to geometrical constraints. Moreover, a consistent picture regarding the impact of directional flow fields on dendrites has not yet emerged: Nguyen-Thi et al. found bending to occur in the direction of the flow, away from the feeding-element-rich melt, and toward the colder region [22]. Similar results were obtained by Nabavizadeh et al. in simulations [18]. On the other hand, Murakami et al. observed the bending of dendrites against the flow direction, toward the hotter region and toward higher feeding-element concentration [45].

A notable difference between those works, however, is the solidification speed of the alloy: While in Murakami's experiment the dendrites grew with around $1 \text{ mm} \cdot \text{s}^{-1}$, the crystallization speed in Nguyen's study was 1000 times slower [22, 45]. As the solidification speed in the present case is of the same order of magnitude, the experiment of Nguyen et al. would well approximate our results, which is supported by the observation that the dendrites in the present research also bend in direction of the fluid flow (see Fig. 5).

Figure 4 Three-dimensional projection color plot of **a** the maximum solidification front growth velocity and **b** the relative increase in solidification front growth velocity varying with d_{flat} (x-axis) and D (y-axis). d_{flat} is the distance between a bubble and the solidification front before it bulges out and D is the bubble diameter at the moment of first deformation of the solidification front. In both panels, different amounts of solved H, respectively, of $5.4 \cdot 10^{17}$ atoms/g (solid squares) and $2.7 \cdot 10^{17}$ atoms/g (empty squares), do not affect this behavior, only the amount of observable events. The color map consists of data points from all four samples. Different solidification parameters did not show any impact on the bubbles; thus, for the convenience of the reader, the authors refrained from using color coding on the data points.



It should be noted that the Marangoni effect and the bulging are not mutually contradictory, as the increase in growth speed due to the insulating effect of the bubble acts on a larger range than the Marangoni effect. The latter would thus only cause a slight depression at the tip of the bulge, coinciding

with the zone of solute enrichment between bubble and dendrites, in which the high Cu-concentration retards the growth of Al-dendrites [17], the differentiating factor between the depression due to solute enrichment and the depression caused by Marangoni flow being the bending of the dendrites.

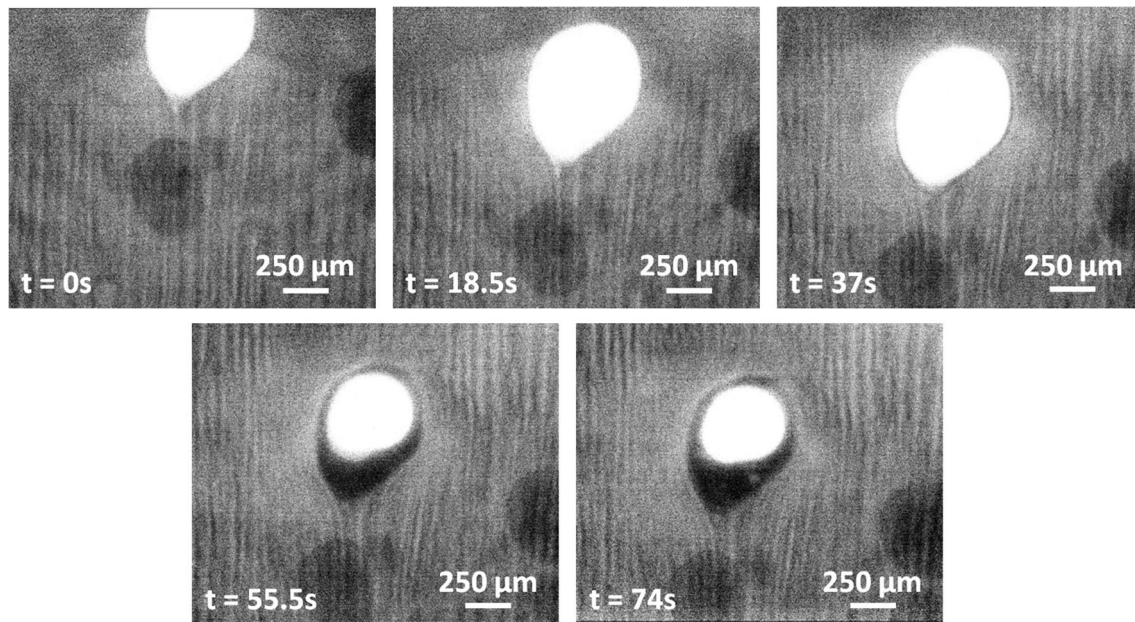


Figure 5 In situ images of sample 2 at different times during solidification. Upward-growing columnar dendrites stop or deviate/bend before coming into contact with a H-bubble in the Al-10%wt.Cu alloy charged with $2.7 \cdot 10^{17}$ H-atoms/g. The

Coronal growth

The engulfment of a gas bubble by a dendritic layer around the gas–liquid interface, similar to heterogeneous nucleation at a solid–liquid interface, was observed and discussed by Xing et al. in situ for organic succinonitrile-based transparent alloys [20]. The dendrite that comes into contact with the bubble is stopped, before a halo of nucleating crystallites engulfs the bubble. Eventually, the influence of the applied thermal gradient causes some of the extrusions to evolve into columnar dendrites that either grow in the direction of the temperature field while the remainder is blocked by the surrounding dendrites, or deviate from the direction of the original dendrites and instead grow a new grain starting from the pore. Our results confirm those findings to be valid not only for organic models, but even for our Al–Cu alloy, determining that the metallic nature of the experimental system does not invalidate this effect.

While pores are generally known as stress concentrators and starting points for cracks, literature tends to evaluate them based only on the size and shape of the pore itself [46]. In the present case, however, it can be seen that the influence of the pore

bubble partly popping at about $t = 50$ s allows for a better contrast of its immediate surroundings. In all images, gravity acts orthogonally through the image plane.

extends on a microscopic scale to a halo-shaped area surrounding it, up to twice the bubble radius. In this region of the sample, the directional dendritic growth is replaced by a zone of disordered crystallization. Macroscopically, an alteration of the original grain structure can occur. This can compromise the mechanical stability if a homogeneous columnar microstructure is desired in an application.

Secondary reactions of the bubbles to the approaching solidification front

As the distance to the solid–liquid interface decreases, one can observe a range of secondary effects on the gas bubbles.

Similar to the phenomenon of interdendritic bubble growth during solidification, which has already been extensively discussed in other publications [6, 7, 11, 12, 37, 47], the gas bubbles in front of the growing dendrites also grow quickly (see Figs. 2 and 3). The effects are the same here as in the aforementioned interdendritic case: Upon crystallization, the H-solubility in the material is greatly reduced, and the H gets rejected from the Al into the melt, where it diffuses toward points of locally lowered partial H-pressure. Existing bubbles thus grow by absorbing the surrounding H. In the interdendritic space, this

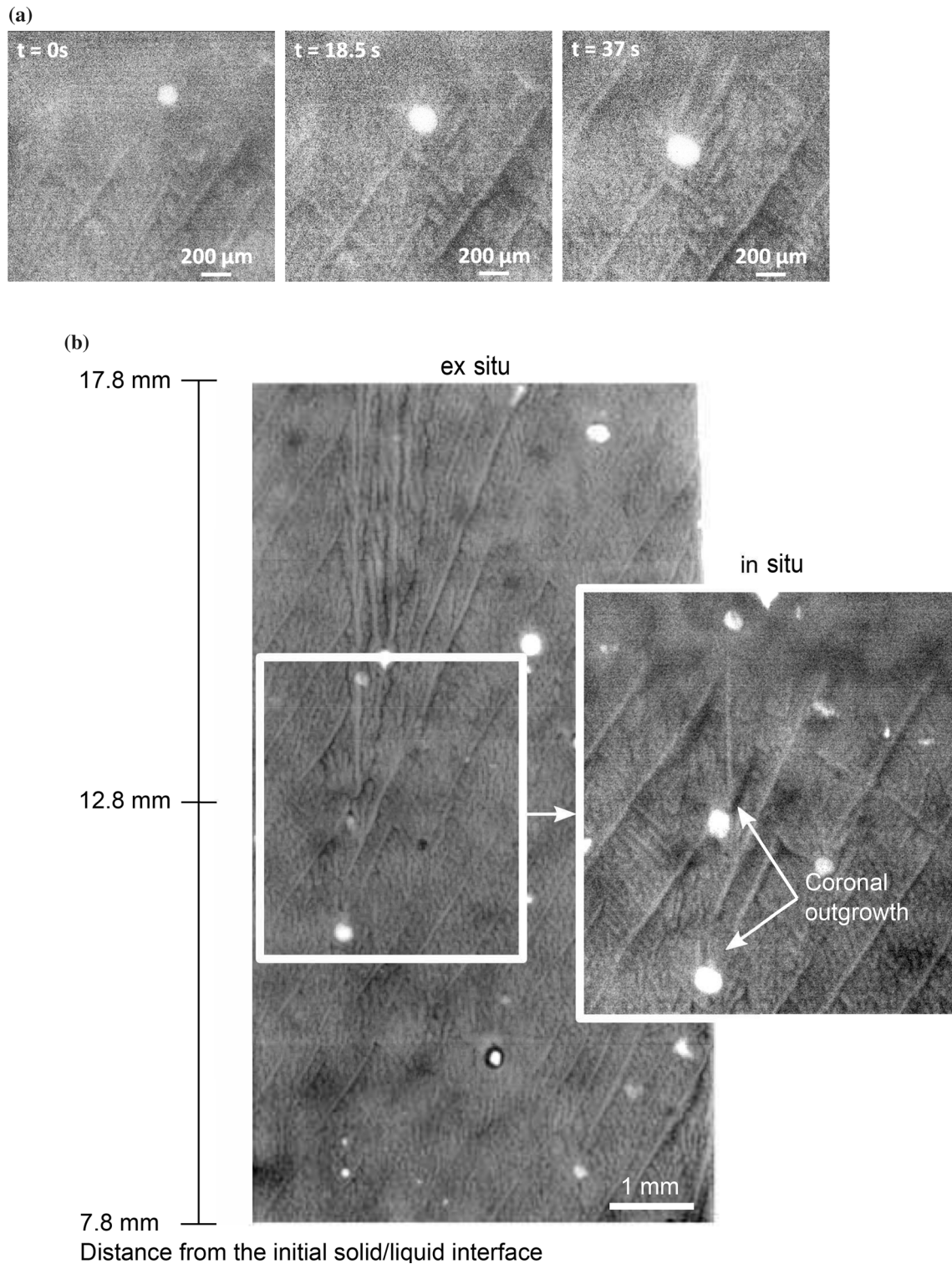


Figure 6 X-radiography image sequence of sample 1 at different times during the solidification, for which the development of coronal outgrowths along the bubble-melt interface in the Al-10%wt.Cu sample loaded with $5.4 \cdot 10^{17}$ H-atoms/g is observed. **a** The discontinuity in upward columnar dendrite growth, covering a ring-shaped area of twice the bubble

diameter surrounding the gas-pore, forms following the direct contact of a dendrite with a H-bubble. Eventually, the outgrowths evolve into dendrites and grow larger. **b** The new dendrites can either grow in the same direction as the initial crystallites or deviate and form a new grain. In all images, gravity acts orthogonally through the image plane.

effect is more pronounced than in the free melt, as the distance to the solid Al-dendrites (where the H rejection takes place) is on the scale of interdendritic spacing, while in the free melt, the distance between bubble and dendrites only decreases gradually upon advancement of the solidification front [37]. Moreover, when comparing bubbles in the melt, close to the solid, to bubbles farther away, multiple factors cause the nearby bubbles to grow faster: Close to the solidification front, the Cu-concentration is higher and, as explained by Anyalebechi [48], increased Cu-content decreases H-solubility, as do the lower temperatures at that position of the sample [49]. Eventually, H being rejected by the solidifying metal leads to a locally increased H-concentration in the melt. The sum of these effects, as well as the out-gassing over time of the supersaturated H, cause more H to agglomerate in the form of bubbles in the vicinity of the solidification front than far away from it. The distance to the solidification front is thus the indirect parameter that affects the growth rate through the direct parameters which scale with the distance. In both Fig. 3a and b, the effect of these combined factors can be observed: The growth rate of the bubble is not constant, as it would be for a purely time-dependent—but not spatially varying—process and instead increases the closer the solid gets to the bubble.

As the solidification front reaches the bubble, an effect analogous to instances of pushing and engulfment of solid particles can be observed, as gas-bubbles are also pushed or engulfed by the solidifying material (see Fig. 2) [50–53]. However, as the bubble itself is a fluid of very low density, the lift forces that are known to be responsible for particle pushing only apply marginally. These lift forces are the Saffman force and the Magnus force [50, 53–56]. The Saffman force acts on a particle in a flow field when there is a gradient in relative flow speed. This is the case when a particle in a flow field is close to a non-moving solid surface, as the flow speed decreases with decreasing distance to the surface. The particle is then pushed away from the surface by the Saffman force. The second lift force, the Magnus force, is generated when particles are rotating, which produces a lift force perpendicular to both the direction of the fluid flow and the axis of rotation. The rotation is induced by the forced convection in front of the dendrite tips due to gravity. The effects of convective flow are, however, strongly reduced for the case of a gas bubble as compared to that of a solid

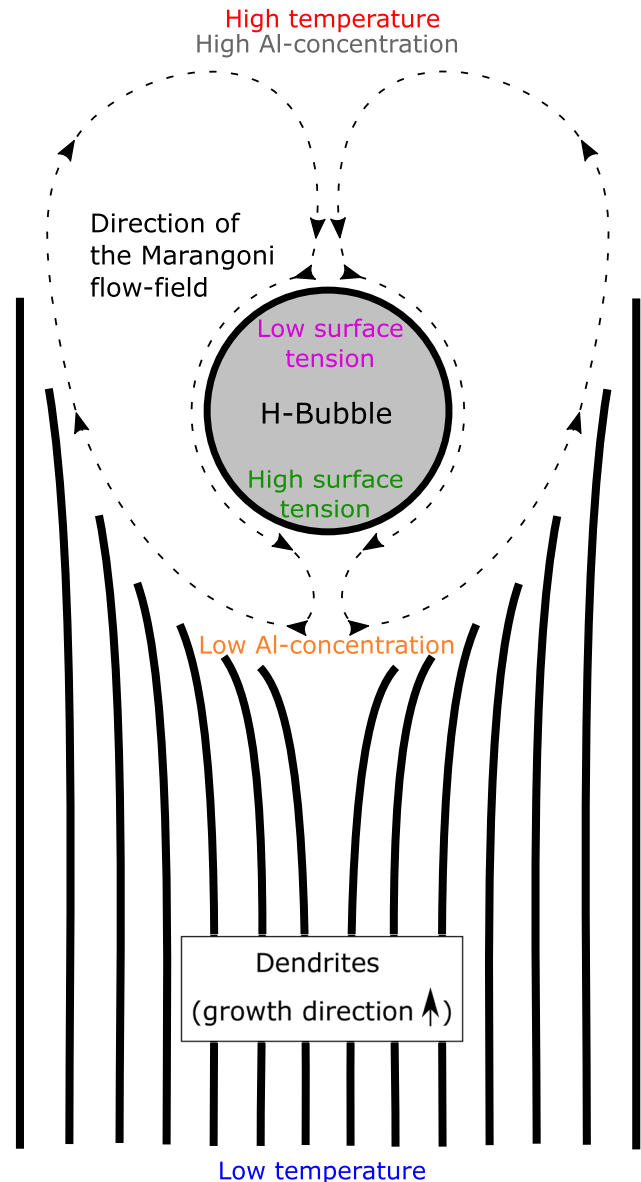


Figure 7 Marangoni flow (dashed lines) surrounding a gas-pore, and its effect on the growth direction of the dendrites under microgravity. The differences in temperature and composition of the Al–Cu melt cause a gradient in surface tension around the bubble. According to the Marangoni effect, liquid flow toward the side of highest surface tension ensues and two flow vortices at the sides of the bubble form. This flow of hot, Al-rich melt causes the dendrites in proximity of the bubble to bend/deviate from their original growth direction. As adapted from [18, 42].

particle: Inducing rotation in a sphere of fluid inside of a second fluid requires transmission of shear forces, which are almost negligible in the case of a gas due to the gas' low viscosity and the reduced convective flow resulting from the horizontal orientation of the sample [50, 53–56].

The bubbles also sporadically display bursts of fast movement in a certain direction upon interacting with, and being partially engulfed by, the advancing solidification front (see Fig. 2 for $t = 74.1$ s). As Han discovered for transparent cyclohexane model alloys, upon being at least partially surrounded by solidifying material, growing bubbles can experience deformation, resulting in an increase in internal pressure [57]. Once the internal pressure becomes large enough, the bubble will then push aside the crystallized material and escape the mushy zone while restoring its own energetically favored round shape. Han coined this process “bubble eruption”.

It has to be noted, however, that Han’s case and the present work are different in that Han’s bubbles are confined to the mushy zone, while in the present experiments, the solidifying material slowly surrounds the bubble. In the present study, the gas-bubbles are thus only “held in place” by a smaller fraction of the engulfing material. This causes the holding force, and consequently the internal pressure of the bubble, to be lower than in Han’s research and explains why the “eruption” in the present experiments is not as explosive and only displaces the bubble by about $50\ \mu\text{m}$, while Han observed distances exceeding $1\ \text{mm}$.

A final reaction was observed in bubbles throughout the whole sample, but especially for bubbles that were close to the solidification front: popping of the bubble, as seen in Fig. 2 for $t = 84.6$ s. Due to the aforementioned increasing growth rate of the bubbles with decreasing distance from the solidification front, small bubbles would grow bigger and pop at the top or bottom face of the sample.

Conclusions

Three major findings have been reported in this paper.

- (i) It was shown that gas bubbles play a noticeable role during directional solidification of metals. The increased thermal gradient ahead of the bubble, resulting from the insulating properties of the gas pocket, directly impacts growth speed and homogeneity of the

solidification front, coinciding with predictions by previous simulations: The solidification front does not remain flat but bulges in the vicinity of the bubbles. The range of this effect was found to be up to $900\ \mu\text{m}$ depending on the size of the bubble, locally increasing solidification speed by up to 350%. Differences to experiments on transparent polymer model alloys could be attributed to the vast disparity in physical properties of metallic samples when compared to organic specimens and highlight the importance of confirming findings from model systems with experimental data from real metallic samples.

- (ii) Results showing dendrites deviating from their original growth direction in front of a H-bubble suggest an influence of the Marangoni effect on the growth of dendrites in the vicinity of a gas bubble, as simulated by Nabavizadeh et al. [18], however, the effect could not be fully validated with the current setup. Follow-up experiments with varying experimental conditions, notably slower solidification rates, as well as different surface energies, are planned. A possible method to vary the surface energy is the use of an Al–Ge alloy instead of Al–Cu: As the surface energy of the alloy increases with increasing Cu-content (boosted Marangoni flow toward dendrites), but decreases with increasing Ge-content (Marangoni flow potentially inhibited), differences in the flow field behavior should be observable when comparing these two alloy systems. To restrict the influence of gravity on the flow fields, microgravity and near-microgravity experiments are planned, as well as trials under standard gravity, to confirm the necessity of microgravity for this setup. Especially for thicker and/or bulk samples, microgravity experiments are expected to yield conclusive results.
- (iii) As a special case of bubble engulfment, the coronal growth effect plays an important role in the solidification process. The resulting

zone of small disordered dendrites obstructs the homogenous growth of the original dendrites and disrupts the columnar microstructure over an even larger range than the gas-pore itself, validating earlier experiments on organic model alloys for their metallic counterparts. Even new grains can nucleate from these coronal outgrowths. The authors suggest mechanical testing on samples featuring pores with coronal growth compared to samples without this effect, to clearly determine the effective impact this phenomenon has on the mechanical properties of the material.

Supplemental Material

As literature sources give H-content in varying units [17, 21, 29–31], equations (1) to (3) provide the conversion-method for comparison of results in different units, where N_A is the Avogadro constant, V_m is the molar volume, n_{apm} expresses the number of atoms per molecule (in the case of H_2 this parameter equals 2), m_i the mass of alloy-element i in the sample, and M_i the molar mass of element i . The subscript STP indicates the assumption of standard conditions for temperature and pressure, respectively, 273.15 K and 1000 hPa [58]. Note that the switch from 1 atm, as standard pressure, to 1000 hPa (= 0.9869 atm), decided by the International Union of Pure and Applied Chemistry in 1982 [59], invalidates the commonly used $V_m = 0.022414 \text{ m}^3 \cdot \text{mol}^{-1}$ in favor of the new standard value of $V_m = 0.022711 \text{ m}^3 \cdot \text{mol}^{-1}$.

$$[H - atoms/g_{Alloy}] = [ppma_{H-atoms}] \cdot N_A \cdot \frac{\sum m_i}{\sum M_i} \cdot 10^{-6} \quad (1)$$

$$= [ppmw_{H-atoms}] \cdot N_A \cdot \frac{\sum m_i}{M_H} \cdot 10^{-6} \quad (2)$$

$$= [ccm_{H_2}/100g_{Al-10\%wt.Cu}]_{STP} \cdot N_A \cdot \frac{n_{apm}}{V_m} \cdot 10^{-2} \quad (3)$$

As can be partially inferred from the formula, each of these notations provides different advantages: $[H\text{-atoms}/g_{Alloy}]$ is a straightforward experiment-centered notation, $[ccm_{H_2}/100g_{Alloy}]_{STP}$ is the most commonly used. As for $[ppmw]_{H\text{-atoms}}$, it correlates well with the commonly used [%wt.] for the elemental composition of the analyzed alloy.

$[ppma]_{H\text{-atoms}}$, on the other hand, is the only notation that allows for the direct comparison of samples with different elemental compositions. This can be seen in Table 2 for the starred entries, where Al-33%wt.Cu features a lower H-content than Al-4.5%wt.Cu for the mass centered units, but when taking into account the actual number of atoms, the H-content in Al-33%wt.Cu is higher.

Specifically, the [ppm] notations have great practical use, however, due to a lack of international norms addressing the exact nomenclature, a vast mix of variants are used by authors, sometimes without any clarification at all on whether atomic parts per million [ppma], or weight parts per million [ppmw] are used, in some works even the syntax of the unit changing midways through the paper. Table 3 gives an overview over the most common notations for [ppm].

Table 2 Overview over H-content in different Al and Al-alloys as adapted from multiple works since 1989.

Composition	H-content				Publication
	[10 ¹⁷ H – atoms/g]	[ccm/100g] _{STP}	[ppma]	[ppmw]	
Al–50 %wt. Cu	0.23	0.044	1.47	0.039	Ichimura et al. (1989) [27]
Al–40 %wt. Cu	0.24–0.85	0.045–0.16	1.38–4.94	0.040–0.14	Ichimura et al. (1989) [27]
Al–33 %wt. Cu	0.16–1.59	0.030–0.30	0.88–8.80	0.027–0.27	Ichimura et al. (1989) [27]
Al–20 %wt. Cu	1.91*	0.36*	10.58*	0.32 *	Anyalebechi (1995) [48]
	0.58–0.85	0.11–0.16	2.95–4.30	0.098–0.14	Lee and Hunt (1997) [12]
Al–15 %wt. Cu	0.29–1.86	0.055–0.35	1.48–9.40	0.049–0.31	Ichimura et al. (1989) [27]
	2.09	0.39	10.26	0.35	Anyalebechi (1995) [48]
Al–10 %wt. Cu	0.69–1.06	0.13–0.20	3.38–5.20	0.12–0.18	Lee and Hunt (1997) [12]
	2.67–5.36	0.50–1.01	12.70–25.48	0.45–0.90	Present work
Al–6.2 %wt. Cu	0.011–1.06	0.0020–0.20	0.050–5.04	0.0018–0.18	Ichimura et al. (1989) [27]
	1.43	0.27	6.81	0.24	Lee and Hunt (1997) [12]
	1.59	0.30	7.56	0.27	Felberbaum and Rappaz (2011) [11]
	1.38–5.36	0.26–1.01	6.56–25.48	0.23–0.90	Werner et al. (2020) [21]
	0.053–0.45	0.0099–0.085	0.25–2.15	0.0088–0.076	Tiryakioğlu (2020) [28]
	0.60–4.78	0.11–0.90	2.78–22.21	0.10–0.80	Kuznetsov and Xiong [60]
Al–4.5 %wt. Cu	3.35	0.63	15.39	0.35	Anyalebechi (1995) [48]
Al–4.5 %wt. Cu–1.4 %wt. Mg	2.17*	0.41 *	10.00*	0.36*	Felberbaum and Rappaz (2011) [11]
	0.36–1.01	0.067–0.19	1.63–4.63	0.059–0.17	Anyalebechi (2013) [31]
Al–1 %wt. Cu	2.70	0.51	12.20	0.45	Felberbaum and Rappaz (2011) [11]
Al–12 %wt. Si	1.34	0.25	6.02	0.22	Tiryakioğlu (2020) [28]
Al–0.25 %wt. Au	0.069	0.013	0.31	0.012	Catalina et al. (2004) [17]
Al (pure)	0.065	0.012	0.29	0.011	Catalina et al. (2004) [17]
	0.00022–0.89	0.000042–0.17	0.001–4.00	0.000037–0.15	Rozenak (2014) [29]

Values in the units used in the respective publication are marked in bold. The starred lines illustrate the problematic of mass-centered units displaying a higher H-atom content, despite there being a lower amount of H-atoms as shown by the [ppma] value

Table 3 Summary of the most common notations for the unit [ppm]

Designation	Unit	Alternative notations found in literature [17, 28, 29, 48, 60, 61]
Parts per million (atomic)	$\left[\frac{\text{Atoms}}{10^6 \text{Atoms}}\right] = [\text{ppma}]$	[ppmat.] [appm] [at.ppm]
Parts per million (weight)	$\left[\frac{\text{kg}}{10^6 \text{kg}}\right] = [\text{ppmw}]$	[ppmw.] [wppm] [wt.ppm] [10 ⁻⁴ %wt.] [10 ⁻⁴ wt.%] [10 ⁻⁴ wt.pct.]

Acknowledgements

The authors would like to thank S. Steinbach and A. Jafarizadeh for the fruitful exchange, and especially M. Kolbe, who not only provided valuable insights but who also kept the imaging facilities in working conditions despite the pandemic. Furthermore, M. J. Püschel's linguistic input was very much appreciated, as was his great help in completing the manuscript.

Funding

Open Access funding enabled and organized by Projekt DEAL.

Compliance with ethical standards

Conflict of interest The authors declare that they have no conflict of interest.

Open Access This article is licensed under a Creative Commons Attribution 4.0 International License, which permits use, sharing, adaptation, distribution and reproduction in any medium or format, as long as you give appropriate credit to the original author(s) and the source, provide a link to the Creative Commons licence, and indicate if changes were made. The images or other third party material in this article are included in the article's Creative Commons licence, unless indicated otherwise in a credit line to the material. If material is not included in the article's Creative Commons licence and your intended use is not permitted by statutory regulation or exceeds the permitted use, you will need to obtain permission directly from the copyright holder. To view a copy of this licence, visit <http://creativecommons.org/licenses/by/4.0/>.

References

- [1] Garbacz-Klempka A, Dlugosz P, Kwak Z, Karczmarek L, Kozana J, Piekos M, Perek-Nowak M (2018) Analysis of a castings quality and metalworking technology. treasure of the bronze age axes. *Arch Foundry Eng* 18:179–185. <https://doi.org/10.24425/123622>
- [2] Han Q, Viswanathan S (2002) Hydrogen evolution during directional solidification and its effect on porosity formation in aluminum alloys. *Metall Mater Trans A* 33:2067–2072. <https://doi.org/10.1007/s11661-002-0038-0>
- [3] Pequet C, Rappaz M, Gremaud M (2002) Modeling of microporosity, macroporosity, and pipe-shrinkage formation during the solidification of alloys using a mushy-zone refinement method: applications to aluminum alloys. *Metall Mater Trans A* 33:2095–2106. <https://doi.org/10.1016/j.actamat.2011.07.005>
- [4] Arnberg L, Mathiesen RH (2007) The real-time, high-resolution x-ray video microscopy of solidification in aluminum alloys. *JOM* 59:20–26. <https://doi.org/10.1007/s11837-007-0099-z>
- [5] Zhang Q, Sun D, Pan S, Zhu M (2020) Microporosity formation and dendrite growth during solidification of aluminum alloys: modeling and experiment. *Int J Heat Mass Transf* 146:118838. <https://doi.org/10.1016/j.ijheatmasstransfer.2019.118838>
- [6] Akamatsu S, Faivre G (1996) Residual-impurity effects in directional solidification: long-lasting recoil of the front and nucleation-growth of gas bubbles. *J de Phys I* 6:503–527. <https://doi.org/10.1051/jp1:1996227>
- [7] Wei PS, Huang CC, Wang ZP, Chen KY, Lin CH (2004) Growths of bubble/pore sizes in solid during solidification—an in situ measurement and analysis. *J Cryst Growth* 270:662–673. <https://doi.org/10.1016/j.jcrysgro.2004.06.039>
- [8] Wei PS, Huang CC, Lee KW (2003) Nucleation of bubbles on a solidification front—experiment and analysis. *Metall Mater Trans B* 34:321–332. <https://doi.org/10.1007/s11663-003-0078-x>
- [9] Wei PS, Hsiao SY (2012) Pore shape development from a bubble captured by a solidification front. *Int J Heat Mass Transf* 55:8129–8138. <https://doi.org/10.1016/j.ijheatmasstransfer.2012.08.054>
- [10] Couper MJ, Neeson AE, Griffiths JR (1990) Casting defects and the fatigue behaviour of an aluminium casting alloy. *Fatigue Fract Eng Mater Struct* 13:213–227. <https://doi.org/10.1111/j.1460-2695.1990.tb00594.x>
- [11] Felberbaum M, Rappaz M (2011) Curvature of micropores in al-cu alloys: an x-ray tomography study. *Acta Materialia* 59:6849–6860. <https://doi.org/10.1016/j.actamat.2011.07.005>
- [12] Lee PD, Hunt JD (1997) Hydrogen porosity in directional solidified aluminium-copper alloys: in situ observation. *Acta Materialia* 45:4155–4169. [https://doi.org/10.1016/s1359-6454\(97\)00081-5](https://doi.org/10.1016/s1359-6454(97)00081-5)
- [13] Murphy AG, Browne DJ, Houltz Y (2016) and R. H. Mathiesen, “In-situ X-ray observations of gas porosity interactions with dendritic microstructures during solidification of al-based alloys,” *IOP Conference series: materials*

- science and engineering*, Vol. 117, pp. 012067. <https://doi.org/10.1088/1757-899x/117/1/012067>
- [14] Campbell J (2003) Castings. Elsevier, Amsterdam. <https://doi.org/10.1016/b978-0-7506-4790-8.x5016-5>
- [15] Mathiesen RH, Arnberg L, Ramsøskar K, Weitkamp T, Rau C, Snigirev A (2002) Time-resolved x-ray imaging of aluminum alloy solidification processes. *Metall Mater Trans B* 33:613–623. <https://doi.org/10.1007/s11663-002-0041-2>
- [16] Sekhar JA, Trivedi R (1991) Solidification microstructure evolution in the presence of inert particles. *Mater Sci Eng: A* 147:9–21. [https://doi.org/10.1016/0921-5093\(91\)90800-3](https://doi.org/10.1016/0921-5093(91)90800-3)
- [17] Catalina AV, Sen S, Stefanescu DM, Kaukler WF (2004) Interaction of porosity with a planar solid/liquid interface. *Metall Mater Trans A* 35:1525–1538. <https://doi.org/10.1007/s11661-004-0260-z>
- [18] Nabavizadeh SA, Eshraghi M, Felicelli SD, Tewari SN, Grugel RN (2019) The marangoni convection effects on directional dendritic solidification. *Heat Mass Transf* 56:1329–1341. <https://doi.org/10.1007/s00231-019-02799-4>
- [19] Han SH, Trivedi R (1994) Primary spacing selection in directionally solidified alloys. *Acta Metallurgica et Materialia* 42:25–41. <https://doi.org/10.1016/j.scriptamat.2006.07.052>
- [20] Xing H, Wang JY, Chen CL, Shen ZF, Zhao CW (2012) Bubbles engulfment and entrapment by cellular and dendritic interfaces during directional solidification. *J Cryst Growth* 338:256–261. <https://doi.org/10.1016/j.jcrysgro.2011.10.047>
- [21] Werner T, Lehmann P, Baumann J, Kargl F, Tyburska-Püschel B (2020) Gas-loading furnace for deuterium-charged alloy-casting. *Rev Sci Instrum* 91:043901. <https://doi.org/10.1063/5.0004356>
- [22] Nguyen-Thi H, Reinhart G, Salloum-Abou-Jaoude G, Browne DJ, Murphy AG, Houlitz Y, Li J, Voss D, Verga A, Mathiesen RH, Zimmermann G (2014) XRMON-GF experiments devoted to the in situ x-ray radiographic observation of growth process in microgravity conditions. *Microgravity Sci Technol* 26:37–50. <https://doi.org/10.1007/s12217-014-9370-4>
- [23] Kargl F, Balter M, Stenzel C, Gruhl T, Daneke N, Meyer A (2011) Versatile compact x-ray radiography module for materials science under microgravity conditions. *J Phys: Conf Ser* 327:012011. <https://doi.org/10.1088/1742-6596/327/1/012011>
- [24] Wriedt HA (1985) The Al-O (aluminum-oxygen) system. *Bull Alloy Ph Diagr* 6:548–553. <https://doi.org/10.1007/bf02887157>
- [25] Wriedt HA (1986) The Al-N (aluminum-nitrogen) system. *Bull Alloy Ph Diagr* 7:329–333. <https://doi.org/10.1007/bf02873001>
- [26] Ganesan S, Poirier DR (1987) Densities of aluminum-rich aluminum-copper alloys during solidification. *J Light Met* 18(4):721–723. <https://arizona.pure.elsevier.com/en/publications/densities-of-aluminumrich-aluminum-copper-alloys-during-solidifi>
- [27] Ichimura M, Sasajima Y, Imabayashi M (1989) Hydrogen solubility in aluminum-copper alloys. *J Jpn Ins Light Met* 39(9):639–645. <https://doi.org/10.2464/jilm.39.639>
- [28] Tiryakioğlu M (2020) The effect of hydrogen on pore formation in aluminum alloy castings: myth versus reality. *Metals* 10:368. <https://doi.org/10.3390/met10030368>
- [29] Rozenak P (2014) States of hydrogen and deuterium in chemically charged high purity aluminum. *J Alloys Compd* 587:800–806. <https://doi.org/10.1016/j.jallcom.2013.10.229>
- [30] Liu H, Bouchard M, Zhang L (1995) An experimental study of hydrogen solubility in liquid aluminium. *J Mater Sci* 30:4309–4315. <https://doi.org/10.1007/bf00361510>
- [31] Anyalebechi PN (2013) Hydrogen-induced gas porosity formation in al-4.5 wt% cu-1.4 wt% mg alloy. *J Mater Sci* 48:5342–5353. <https://doi.org/10.1007/s10853-013-7329-2>
- [32] American Society for Testing and Materials (2017) E3–11: Standard guide for preparation of metallographic specimens. ASTM International, West Conshohocken, PA. <https://doi.org/10.1520/E0003-11R17>
- [33] Zimmermann G, Pickmann C, Hamacher M, Schaberger-Zimmermann E, Neumann-Heyme H, Eckert K, Eckert S (2017) Fragmentation-driven grain refinement in directional solidification of AlCu10wt-% alloy at low pulling speeds. *Acta Materialia* 126:236–250. <https://doi.org/10.1016/j.actamat.2016.12.063>
- [34] Browne DJ et al. (2017) Overview of in situ x-ray studies of light alloy solidification in microgravity. In: Solanki K, Orlov D, Singh A, Neelameggham N (eds) *Magnesium Technology 2017*. The Minerals, Metals & Materials Series. Springer, Cham. https://doi.org/10.1007/978-3-319-52392-7_80
- [35] Mullins WW, Sekerka RF (1964) Stability of a planar interface during solidification of a dilute binary alloy. *J Appl Phys* 35:444–451. <https://doi.org/10.1063/1.1713333>
- [36] Bechhoefer J (2008) Solidification of viscous melts: the interplay of nano- and macroscopic phenomena. *Int J Nanotechnol* 5:1121. <https://doi.org/10.1504/ijnt.2008.019834>
- [37] Karagadde S, Sundarraj S, Dutta P (2012) A model for growth and engulfment of gas microporosity during aluminum alloy solidification process. *Comput Mater Sci* 65:383–394. <https://doi.org/10.1016/j.commatsci.2012.07.045>
- [38] Yemmou M, Azouni MA, Casses P, Pétré G (1993) Thermal aspects of particle engulfment by a solidifying front. *J Cryst*

- Growth 128:1130–1136. [https://doi.org/10.1016/s0022-0248\(07\)80111-4](https://doi.org/10.1016/s0022-0248(07)80111-4)
- [39] Sergeev OA, Shashkov AG, Umanskii AS (1982) Thermo-physical properties of quartz glass. *J Eng Phys* 43:1375–1383. <https://doi.org/10.1007/bf00824797>
- [40] Mangum BW (1983) The succinonitrile triple-point standard: a fixed point to improve the accuracy of temperature measurements in the clinical laboratory. *Clin Chem* 29:1380–1384. <https://doi.org/10.1093/clinchem/29.7.1380>
- [41] Giordanengo B, Benazzi N, Vinckel J, Gasser JG, Roubi L (1999) Thermal conductivity of liquid metals and metallic alloys. *J Non-Crystalline Solids* 250–252:377–383. [https://doi.org/10.1016/s0022-3093\(99\)00268-9](https://doi.org/10.1016/s0022-3093(99)00268-9)
- [42] Namura K, Nakajima K, Suzuki M (2018) Investigation of transition from thermal- to solutal-marangoni flow in dilute alcohol/water mixtures using nano-plasmonic heaters. *Nanotechnology* 29:065201. <https://doi.org/10.1088/1361-6528/aaa260>
- [43] O’Shaughnessy SM, Robinson AJ (2009) Numerical investigation of bubble-induced marangoni convection. *Ann N Y Acad Sci* 1161:304–320. <https://doi.org/10.1111/j.1749-6632.2008.04332.x>
- [44] Schmitz J, Brillo J, Egry I, Schmid-Fetzer R (2009) Surface tension of liquid al-cu binary alloys. *Int J Mater Res* 100:1529–1535. <https://doi.org/10.3139/146.110221>
- [45] Murakami K, Fujiyama T, Koike A, Okamoto T (1983) Influence of melt flow on the growth directions of columnar grains and columnar dendrites. *Acta Metallurgica* 31:1425–1432. [https://doi.org/10.1016/0001-6160\(83\)90012-3](https://doi.org/10.1016/0001-6160(83)90012-3)
- [46] Cáceres CH, Selling BI (1996) Casting defects and the tensile properties of an AlSiMg alloy. *Mater Sci Eng: A* 220:109–116. [https://doi.org/10.1016/s0921-5093\(96\)10433-0](https://doi.org/10.1016/s0921-5093(96)10433-0)
- [47] Dantzig JA, Rappaz M (2016) *Solidification*. EPFL Press, Lausanne. <https://www.epflpress.org/product/501/9782889142071/solidification>
- [48] Anyalebechi PN (1995) Analysis of the effects of alloying elements on hydrogen solubility in liquid aluminum alloys. *Scripta Metallurgica et Materialia* 33:1209–1216. [https://doi.org/10.1016/0956-716x\(95\)00373-4](https://doi.org/10.1016/0956-716x(95)00373-4)
- [49] Opie WR, Grant NJ (1950) Hydrogen solubility in aluminum and some aluminum alloys. *JOM* 2:1237–1241. <https://doi.org/10.1007/bf03399138>
- [50] Friedrich J, Reimann C, Jauss T, Cröll A, Sorgenfrei T (2016) Interaction of SiC particles with moving solid-liquid interface during directional solidification of silicon. *J Cryst Growth* 447:18–26. <https://doi.org/10.1016/j.jcrysgro.2016.04.061>
- [51] Lierfeld T, Kolbe M, Eggeler G, Herlach DM (2008) Interaction of small ceramic particles with a dendritic solidification front. *Adv Eng Mater* 10:547–553. <https://doi.org/10.1002/adem.200700357>
- [52] Mukherjee S, Stefanescu DM (2004) Liquid convection effects on the pushing-engulfment transition of insoluble particles by a solidifying interface: part i. analytical calculation of the lift forces. *Metall Mater Trans A* 35:613–621. <https://doi.org/10.1007/s11661-004-0373-4>
- [53] Takemura F, Takagi S, Magnaudet J, Matsumoto Y (2002) Drag and lift forces on a bubble rising near a vertical wall in a viscous liquid. *J Fluid Mech* 461:277–300. <https://doi.org/10.1017/s0022112002008388>
- [54] Spurk HJ, Aksel N (2008) *Fluid mechanics*. Springer, Berlin. <https://doi.org/10.1007/978-3-540-73537-3>
- [55] Stone HA (2000) Philip saffman and viscous flow theory. *J Fluid Mech* 409:165–183. <https://doi.org/10.1017/s0022112099007697>
- [56] Rastello M, Marié J-L, Grosjean N, Lance M (2009) Drag and lift forces on interface-contaminated bubbles spinning in a rotating flow. *J Fluid Mech* 624:159–178. <https://doi.org/10.1017/s0022112008005399>
- [57] Han Q (2006) Motion of bubbles in the mushy zone. *Scr Mater* 55:871–874. [https://doi.org/10.1016/0956-7151\(94\)90045-0](https://doi.org/10.1016/0956-7151(94)90045-0)
- [58] IUPAC. Standard Temperature and Pressure. In: Compendium of Chemical Terminology, 2nd ed. (the “Gold Book”). Compiled by McNaught AD and Wilkinson A (eds) Blackwell Scientific Publications, Oxford (1997). Online version (2019-) created by S. J. Chalk. ISBN 0-9678550-9-8. <https://doi.org/10.1351/goldbook.s06036>
- [59] Cox JD (1982) Notation for states and processes, significance of the word standard in chemical thermodynamics, and remarks on commonly tabulated forms of thermodynamic functions. *Pure Appl Chem* 54:1239–1250. <https://doi.org/10.1351/pac198254061239>
- [60] Kuznetsov AV, Xiong M (2002) Dependence of microporosity formation on the direction of solidification. *Int Commun Heat Mass Transf* 29:25–34. [https://doi.org/10.1016/s0735-1933\(01\)00321-9](https://doi.org/10.1016/s0735-1933(01)00321-9)
- [61] Boeira AP, Ferreira IL, Garcia A (2006) Modeling of macrosegregation and microporosity formation during transient directional solidification of aluminum alloys. *Mater Sci Eng: A* 435–436:150–157. <https://doi.org/10.1016/j.msea.2006.06.003>

Publisher’s Note Springer Nature remains neutral with regard to jurisdictional claims in published maps and institutional affiliations.